Visual observation of meteorite ablation in plasma wind tunnel experiments

F. Grigat, S. Loehle, J. Vaubaillon, P. Matlovič, J. Tóth

Icarus 422 (2024) 116249

Contents lists available at ScienceDirect

Icarus

journal homepage: www.elsevier.com/locate/icarus

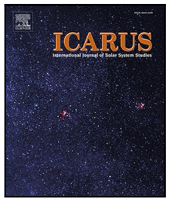

Visual observation of meteorite ablation in plasma wind tunnel experiments

F. Grigat [a,*], S. Loehle [a], J. Vaubaillon [b], P. Matlovič [c], J. Tóth [c]

[a] High Enthalpy Flow Diagnostics Group, Institute of Space Systems, University of Stuttgart, Pfaffenwaldring 29, 70569 Stuttgart, Germany
[b] IMCCE, Observatoire de Paris, PSL, 77 Av. Denfert Rochereau, Paris, 75014, France
[c] Faculty of Mathematics, Physics and Informatics, Comenius University, Bratislava, Slovakia

ARTICLE INFO

Keywords:
Meteorites
Image processing
Meteors

ABSTRACT

A set of 28 different meteorites was tested in 32 ablation experiments in the plasma wind tunnel PWK1 at the Institute of Space Systems. All meteorites were exposed to the same flow condition in consecutive experiments. This paper presents the detailed analysis of high-resolution images taken by DSLR cameras during 26 experiments on 22 different meteorites. It is seen that the ablation behavior of the meteorites differs in the way the material melts and flows downstream. While some meteorites appeared more viscous and most material remained connected to the main body, other samples suggest a much lower viscosity as the material was carried downstream and released droplets to the flow. Most droplets of molten material were seen for the two most carbon rich samples from meteorites Murchison and Dhofar 1575. The release of blue colored particles was observed for several meteorites, independent of the viscosity. In contrast to the molten droplets, the blue particles also traveled up to a few millimeters upstream. The abundance of these blue particles is linked to the iron content. Close to no particles or droplets were observed for achondritic samples.

1. Introduction

Every day between 50 and 100 t of meteoroids enter the atmosphere of the Earth (Flynn, 2002). In addition to the study of potential risks through meteoroids a focused effort is also undertaken for the investigation of meteorites as a possible source for organic compounds, which might have contributed to the evolution of life on Earth (Park and Brown, 2012; Jenniskens, 2006). The observation of meteors presents a key aspect of research dedicated to this field (Jenniskens et al., 2016), supported by similarly important analyses of meteorites collected from the ground after their entry. Remote observations using optical methods are used as a means to learn about their characteristics. Remote observations are conducted in very different frequency intervals, from UV light to radio observation networks. In the present study, we only consider visible light, i.e. 400–700 nm, and the term *remote* means the visible only. Most observed meteoroids are vaporized during entry, making a post-flight material analysis impossible (Flynn, 2002). Among the meteorites that are found, on the other hand, few were observed during entry. Ground experiments of collected meteorite samples offer a suitable method to close the gap between remote observations and post-flight analyses (Loehle et al., 2017). Wind tunnel experiments with meteoroid substitutes, basalt and gabbro, have been conducted already in 1967 by Shepard et al. (1967). The authors describe the visual impression of the melting, vaporization, and fragmentation. It was suggested that the behavior is affected by the varying viscosity of the different samples tested. In recent years, there has been an increased interest in ground tests similar to our setup from 2017 (Agrawal et al., 2018; Helber et al., 2019; Panerai et al., 2021), though the number of conducted test campaigns was quite low.

From 2020 to 2022, we, i.e. the High Enthalpy Flow Diagnostics Group (HEFDiG), conducted three campaigns of meteorite testing in the plasma wind tunnel PWK1 at the Institute of Space Systems (IRS) under aerothermal loads representative of an actual atmospheric entry. A detailed description of the test campaign and a discussion of the investigations with respect to previous similar work in the literature is presented by Tóth et al. (2023) and Loehle et al. (2023). In addition to several emission spectroscopic setups (Loehle et al., 2023; Pisarčíková et al., 2023) and thermographic cameras (Leiser et al., 2023) multiple digital single-lens reflex (DSLR) cameras were used for high-resolution visual investigation of the meteorite ablation during the experiment. The focus of this paper is the analysis of the DSLR imaging. The motivation for using the DSLR cameras was to investigate general ablation mechanisms of the meteorites as well as the study of processes that occur on a small spatial scale. This kind of data is a valuable addition to the sets of remote observation data from actual meteors, where small spatial features cannot be resolved. Thus, a main motivation of

* Corresponding author.
E-mail address: fgrigat@irs.uni-stuttgart.de (F. Grigat).
URL: https://www.hefdig.com (F. Grigat).

https://doi.org/10.1016/j.icarus.2024.116249
Received 24 April 2023; Received in revised form 31 July 2024; Accepted 1 August 2024
Available online 8 August 2024

this paper is to provide a visual reference for the meteorite research community.

The visual observation of a *shooting star* in the laboratory can rely only on some obvious features if no quantitative measure is available. As will be shown, the meteorite samples show a distinguishable melting and/or droplet development behavior. We attribute this to their rheological differences. Theoretically, the viscosity is the variable for glassy materials to be determined. In geology, this is usually derived from the material composition of the sample. Many numerical models for meteoroid entry simulations rely on the ablation behavior description of Bethe (1959). It is described that the interaction of the glassy material of a meteorite with the hot gas flow is negligible with respect to the liquid motion. The reason is that the glassy material has a very high viscosity compared to the boundary layer gas. The developing vapor, however, interacts with the flow and has a considerable effect on the boundary layer properties. For the present analysis, this means that we can observe the development of the melting meteorite rather independently from a potential consideration of the effect on the flowfield, or – vice versa – the high-enthalpy gas flow which is the same for all samples has only a minor effect on the development of the melt of the meteorite sample. Thus, the melting behavior, i.e. the visual observation of the development of the heated sample can be considered an effect of the bulk material property of the samples. The physical property showing the behavior of a liquid glassy material is the viscosity. Therefore, our logic in this paper is that the samples showing different melting behavior is related to the viscosity. A possible effect of more volatile components possibly present in some of the samples, e.g. potassium or sodium, can be neglected in this regard, because their contribution is too small to have a considerable effect (Loehle et al., 2023).

A different set of samples fragmenting quickly into several smaller fragments is related to the effect we call *spallation* in atmospheric re-entry thermophysics (Grigat et al., 2022). The incoming heat is generating a large amount of thermal stress that disintegrates some samples. These samples do not melt. Meteorite samples under this category are not considered to be affected by viscosity.

2. Experimental setup

A detailed description of the experimental setup, the testing strategy and ground-to-flight comparability are described in detail in Loehle et al. (2023). The PWK1 facility consists of a vacuum vessel with a length of 5 m and a diameter of 2 m. The magnetoplasmadynamic arcjet generator RD5 is mounted on the movable front lid of the vessel. The flow condition chosen for the experiments in this paper is representative of the entry of a spherical object with a diameter of 34.8 mm at a velocity of 11.7 km s^{-1} at an altitude of 80 km (Loehle et al., 2023). The flight parameters are based on the re-entry of the Hayabusa capsule in 2010 (Loehle et al., 2012). This condition has been investigated extensively in the past and was therefore chosen for this campaign as reference data are available. Meteoroid entries occur between 10 km/s and 70 km/s, so this flow condition is the lower limit of real meteoroid entries. The ground-to-flight comparability is based on the concept of local heat transfer simulation (LHTS) (Kolesnikov, 1999). The flow conditions are given in Table 1. The resulting heat flux based on a cold wall copper heat flux measurement is given additionally.

Before each experiment, the sample was moved to the side for the facility startup. As soon as the desired flow condition was set, the sample was moved to the center of the plasma flow, which marked the beginning of the experiment. The experiments lasted between 2 and 10 s and ended with the shut-off of the plasma generator. In some cases the entire meteorite was melted and all material removed before the plasma generator was shut off. Other experiments were stopped earlier to allow for a post-test analysis of the sample.

In all three test campaigns, a DSLR camera of type Canon EOS 5DSR was mounted on top of the facility. The object distance was approximately 2.5 m. The camera was equipped with a zoom lens with a focal length of 150 to 600 mm and a 2× teleconverter. The focal length was set to 863 mm in the second campaign and to 1200 mm in the first and third campaigns. The resulting nominal resolution of 13 µm px^{-1} and 10 µm px^{-1} presents an unprecedented level of detail for visual analysis of the ablation behavior of meteorites during ground testing. Together with the short exposure times of 125 µs, it can be guaranteed that the seen effects are not due to some smearing during acquisition.

Table 1
Plasma wind tunnel condition (Loehle et al., 2012).

Parameter	Value
Mass flow $\dot{m}$	18.0 g/s
Ambient pressure p_∞	16.6 hPa
Total pressure p_{tot}	24.3 hPa
Arc current I	1220 A
Arc voltage U	133 V
Electronic power P	162 kW
Probe position	x = 270 mm, y = 0 mm
Mass-specific enthalpy h	70 MJ/kg
Heat Flux q''	**16 MW/m^2**

The intensity variation between bright molten material and relatively cold meteorite regions poses a challenge to capture all details with the DSLR cameras. The cameras were set to auto-exposure bracketing mode, to account for these extreme demands towards the dynamic range. This allowed to take photos with three varying apertures in a series. Exposure time was set to 125 µs in all experiments. In this mode, the images were taken in bursts of three exposures at a frame rate of 5 Hz with a short break between each burst. This resulted in an overall frame rate of approximately 4 to 4.5 Hz at a sufficiently high dynamic range for the observation of melting details and fragmentation.

3. Samples

A total of 32 experiments were conducted on samples from 28 different meteorites. High-resolution DSLR images are available for 26 experiments. The samples varied slightly in shape, size, and mass. Most samples were machined to cylinders with a diameter of 10 mm and a length of 10 mm. However, the brittleness of some samples did not allow proper machining, leading to irregular shapes in some cases. The samples were glued or clamped to a copper screw that was attached to a water-cooled brass probe with a solid copper head.

An overview of the classifications and compositions of the meteorites tested was given by Leiser et al. (2023) and is reprinted in Table 2. Tóth et al. (2023) provide a comprehensive overview of all experiments and samples.

4. Results

The following two subsections provide the results of the analysis of the DSLR-data. Sample pictures are shown in Figs. 1 to 7.

The first analysis is carried out to categorize the behavior of the samples. From the visual inspection of the experiments with the DSLR cameras, there were three different types of behavior apparent: (1) longer streaks of material still connected to the actual sample on the holder, (2) samples with molten droplets realeased from the main fragment and (3) samples with small quickly released fragments. We consider the first two phenomena as an effect of the different viscosities of the sample, while the third is due to a rather weak conglomerate of elements, which do not behave as glassy as the samples of the first two categories.

Figs. 1–7 show DSLR images of all tested meteorites. For each sample two images are shown: One from the start of the experiment and one close to the end. The total time of individual experiments was different, depending on the sample material. However, the surface temperature

Table 2
Classification and bulk composition in wt% of the tested meteorites separated by test campaign. For these samples average bulk composition for the respective meteorite class was used.
Source: Table reprinted with permission from Leiser et al. (2023).

Code	Name	Classification	Fe	Si	Mg	Ca	Al	Ref.
KOS	Kosice	H5	28.86	16.51	13.8	1.58	1.07	Ozdín et al. (2015)
BUZ	Buzzard Coulee	H4	27.5	16.9	14.0	12.3	11.3	[a]
PUL	Pultusk	H5	27.21	16.97	14.14	1.25	1.18	Phelan et al. (2022)
RAG	Ragland	LL3	20	19.25	13.3	1.32	1.24	Recca et al. (1986)
KNY	Knyahinya	LL5	20.8	18.75	15	1.33	1.28	Kallemeyn et al. (1989)
CHE	Chelyabinsk	LL5	19.2	20.5	14.5	1.31	1.35	Kirillov et al. (2022) and Phelan et al. (2022)
ALL	Allende	CV	23.16	15.94	15.47	1.84	1.82	Jarosewich et al. (1987) and Kusuno et al. (2013)
NWA	NW Africa 869	L5	22.11	18.25	14.54	1.44	1.09	Metzler et al. (2011) and Phelan et al. (2022)
KLJ	Kheneg Ljouad	LL 5/6	18.5	18.9	15.3	13	1.19	[a]
MUR	Murchison	CM	22.24	12.92	10.94	1.14	1.14	Jarosewich (1971) and Phelan et al. (2022)
DHO	Dhofar 1575	Ureilite	14.76	21.24	21.18	0.77	0.26	[a]
NCO	Norton County	Aubrite	1.67	24.85	24.47	1.33	0.38	Easton (1985)
SAR	Sarcicisek	Howardite	14.5	23.75	9.92	5.81	4.5	Unsalan et al. (2019)
STA	Stannern	Eucrite	13.95	23.12	4.21	7.61	6.49	McCarthy et al. (1973) and Kitts and Lodders (1998)
BIL	Bilanga	Diogenite	10.5	25.78	17.91	0.69	0.46	Barrat et al. (2008) and Kusuno et al. (2013)
MJO	Mount Joy	Octahedrite	92.72	1.09	0	0	0	Lewis and Moore (1971) and Wasson (1969)
LAN	Lancé	CO	25.33	15.89	14.43	1.68	1.43	Kusuno et al. (2013)
LUN	NW Africa 11303	Lunar brecchia	3.31	20.02	2.08	11.86	15.65	[a]
MIN	Mincy	Mesosiderite	11.2	22.19	11.02	3.78	3.54	Mittlefehldt et al. (1979) and Simpson and Ahrens (1977)
MOC	Mocs	L5	22.49	18.25	15.29	1.27	1.13	Miura et al. (1995) and Mason and Wiik (1961)
EAG	Eagle	EL	23.19	20.19	14.43	0.54	1.46	Olsen et al. (1988) and Phelan et al. (2022)
TIS	Tissint	Shergottite	15.34	21.6	10.31	4.65	2.57	Herd et al. (2013)

[a] No data composition was available for meteorites.

established a constant value within the short (about 4 to 5 s) exposure (see Leiser et al., 2023). In the figures, the samples are organized according to the visual appearance of *melting* and *fragmentation*. Some samples appear as if their molten shape is less elongated in the downstream direction. Other samples show a more severe flow of the melt downstream. The last group of samples show the molten layer being transported downstream rapidly in the form of tiny droplets. These different behaviors are attributed to the material's rheology, because the main mechanism to release material is known to be shear forces. The samples are arranged according to this melting behavior: Figs. 1 and 2 show similar behavior, i.e. the molten material sticks elongated to the main body, Figs. 3 to 6 summarize the medium behavior, i.e. the molten material is thinned out and transported further downstream and Fig. 7 summarizes the samples where material particles were released. If the melting behavior is related to viscosity, medium viscosity materials clearly outnumber the other types. Interestingly, only five out of 22 samples were fragile enough to quickly release particles. The released particles furthermore appear colder than the molten droplets seen in the medium and high viscosity. The blueish appearance of cold fragments is attributed to spalled particles at the surface which is discussed in the next section.

Several approaches known from literature were tried to relate the observation to known physical properties of the samples. The melting behavior was tried to be analyzed based on the change of the shape, which did not yield meaningful results for the fragments considered here. The intensity ratios between the front side and the melt in the back were analyzed, too, but no significant correlations were found. For the melt, several empirical models from geology research for the viscosity of melt were assessed (Hui and Zhang, 2007; Giordano et al., 2008), but applying these models to meteorite samples led to viscosity estimates varying by several orders of magnitude and were partly unphysical. The models are based on the analysis of the oxide content. However, it is the minerals that should be considered, since they drive the physical properties. The oxides – as taken in numerical models – are actually misleading, since it gives the impression that the oxides correspond to something physical in the meteorite [private communication Prof. Dan Britt, University of Central Florida (UCF)]. A better knowledge of the mineralogy of the meteorite samples and a suitable viscosity model is required for a theoretical comparison. As the bulk strength and viscosity is highly dependent on the mineralogy of the specific samples, the models based on oxides are not applicable for the purpose of this paper. Extending such a database is beyond the scope of this paper. However, the conclusion drawn here, that the rheology of the samples lead to a grouping of the samples holds, independently from the theoretical description.

Figs. 1 and 2 show meteorite samples for which the ablation behavior corresponds to a higher viscosity sample. The droplets are characterized by long molten material streaks, which remained attached to the main sample body for the duration of the experiment. While the front parts of the samples show many pores with significant intensity differences between the pores and their surrounding material, the molten material in the back is notably brighter than the front and the surface of the droplets appears homogeneous. The brightness in the back of the sample is most likely the result of a higher temperature as the hot material is moved downstream and fewer *cold* pores are present in the back. Though water was used during the cutting of the meteorite samples before the experiments, the pores are unlikely to stem from boiling of remaining water. While hydrogen line emission was seen in spectral measurements during the experiments with hydrated minerals, no hydrogen emission was seen in other samples, even those prepared using water. The pores, on the other hand, are visible for all samples, including those that were machined without the use of water. Possibly, it is boiling of the material itself.

Figs. 3–6 show samples that exhibit a less viscous behavior. Long clusters of molten material form and are released from the main fragment. Again, in most cases the material flowing downstream appears brighter than the material in the front. Most of the tested meteorite samples were observed with this intermediate viscosity behavior. Although a clear distinction between the high viscosity samples and the medium viscosity sample is seen, the calculation of a thermophysical difference is not straight forward. One reason is that these experiments are the very first aerothermal testing of a comprehensive set of samples. So far, a thermophysical characterization of samples was not required since it could not be applied.

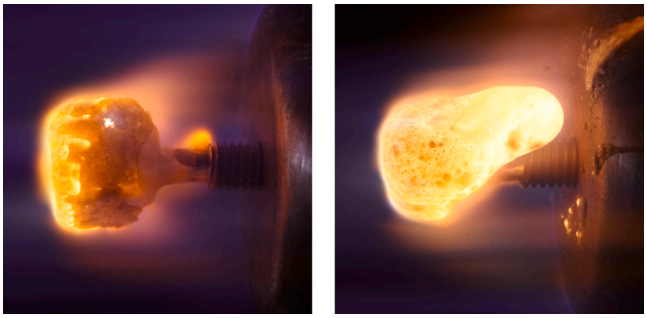

(a) NCO_1 Start (b) NCO_1 End

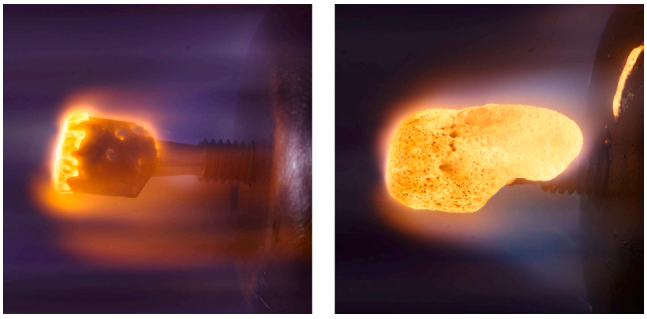

(c) KLJ_1 Start (d) KLJ_1 End

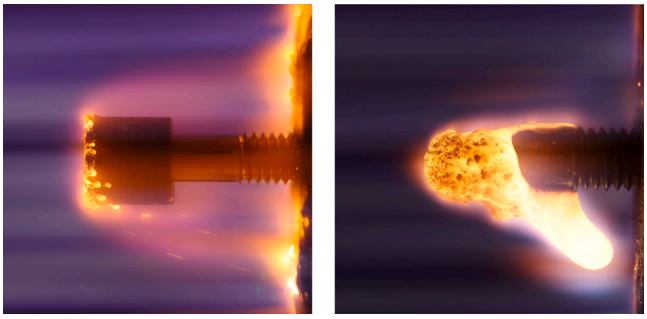

(e) RAG_1 Start (f) RAG_1 End

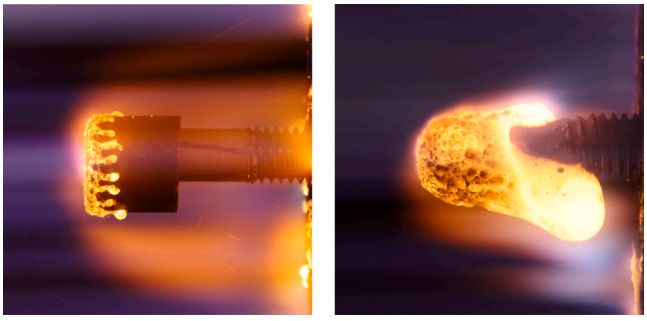

(g) RAG_2 Start (h) RAG_2 End

Fig. 1. High viscosity samples.

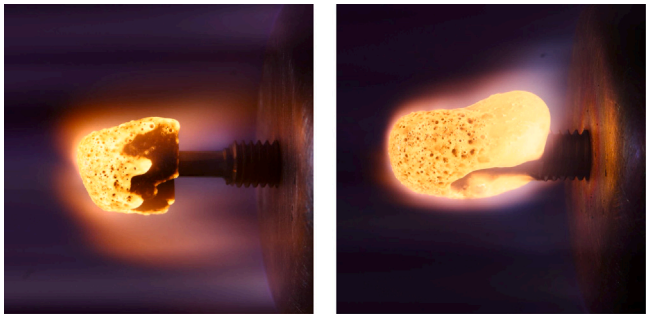

(a) SAR_1 Start (b) SAR_1 End

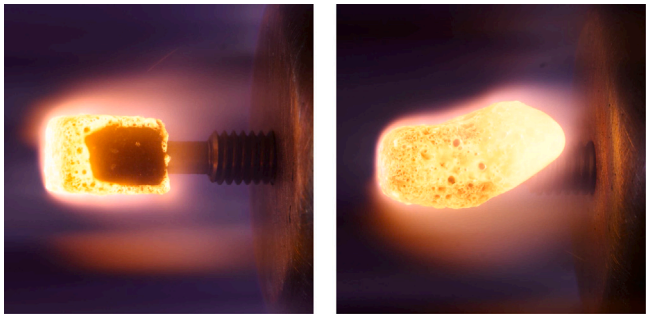

(c) STA_1 Start (d) STA_1 End

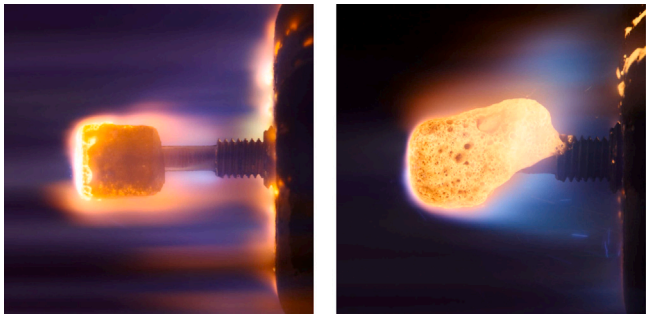

(e) ✻ MOC_1 Start (f) ✻ MOC_1 End

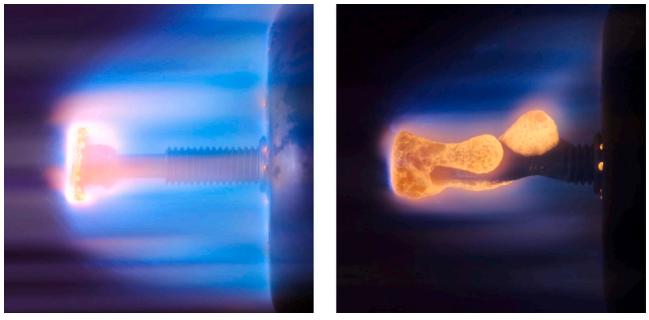

(g) ✻ EAG_1 Start (h) ✻ EAG_1 End

Fig. 2. High viscosity samples (continued from Fig. 1). The symbol ✻ indicates the observation of blue particles in the experiment.

Fig. 7 depicts images of the five samples which released small particles when exposed to the high temperature flow field. While the surfaces of the molten meteorites in Figs. 1 and 5 appear rather smooth, the surface of DHO_1 and MUR_1 is coarse. Material that melts on the surface of these samples is detached easily through shear forces from the flow compared to the other test samples. It is important to note that the most carbon rich samples are in this data set (DHO and MUR). The carbon content of the Murchison sample is estimated at 2.7% (Pearson et al., 2006) and Ureilites like Dhofar 1575 may have carbon contents up to 8% (Goodrich et al., 2015). The other carbonaceous samples Allende and Lance, however, have an estimated carbon content of only 0.27% and 0.65%, respectively (Pearson et al., 2006). In conclusion, the carbon content is an indicator of how fragile samples are. If this is related to the real meteor observation, a quick fragmentation might indicate a high carbon content.

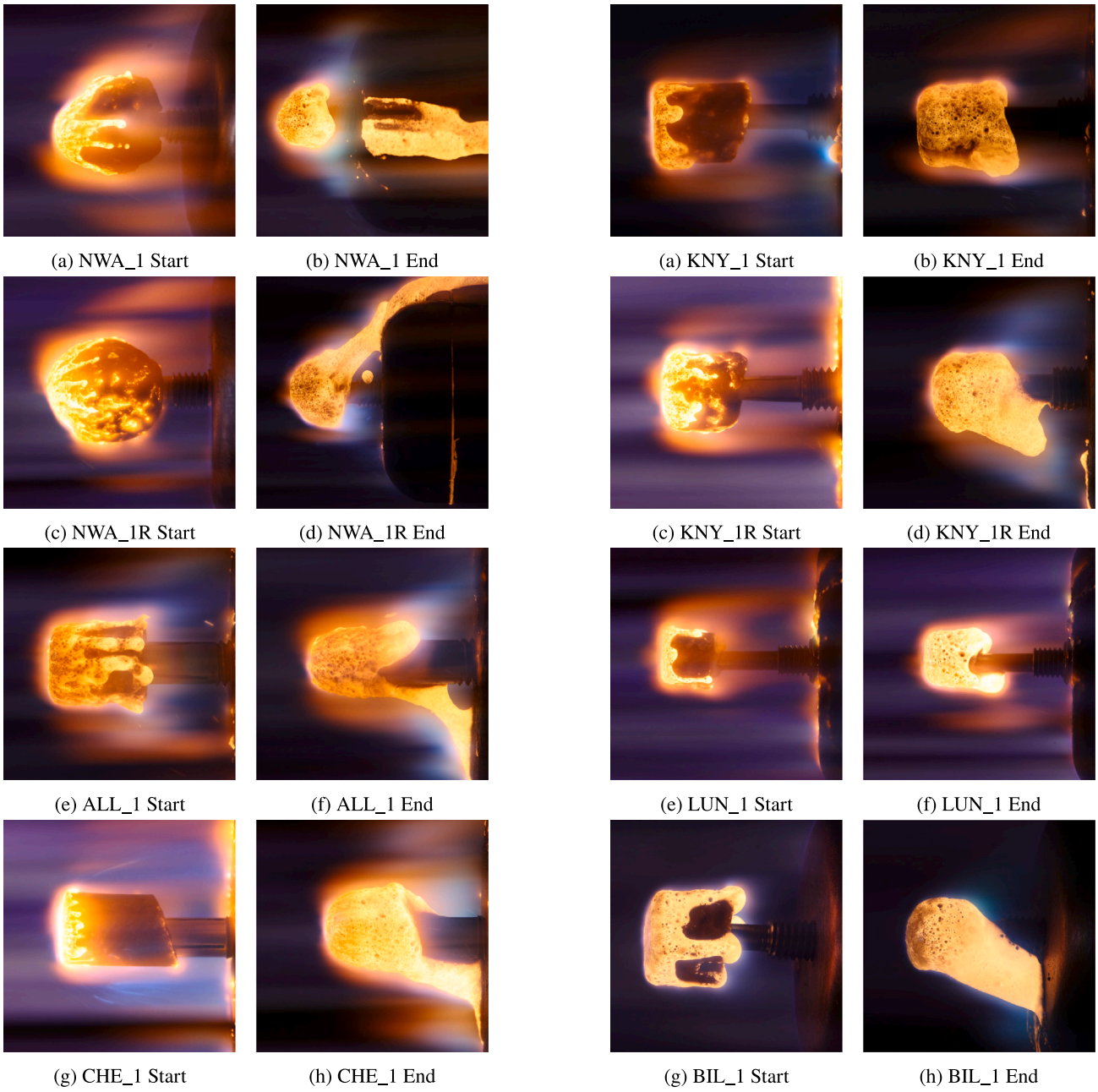

Fig. 3. Medium viscosity samples.

Fig. 4. Medium viscosity samples (continued from Fig. 3).

Table 3
Samples for which blue particles were observed.

Code	Name	Classification
LAN	Lancé	CO
BUZ_1	Buzzard Coulee	H4
BUZ_1R	Buzzard Coulee	H4
EAG	Eagle	EL
KOS_2	Kosice	H5
KOS_3	Kosice	H5
MIN	Mincy	Mesosiderite
MOC	Mocs	L5
MJO	Mount Joy	Octahedrite
PUL	Pultusk	H5

5. Observation of ejected particles

The number of small, often blue glowing particles that are ejected from the surface is very different between the observed samples. The effect is most visible in Fig. 7(f). Unlike the droplets of molten material, these blue particles also travel several millimeters upstream after being released from the front surface. This effect is known from aerospace problems as the *spallation* of material. It is unrelated to the molten material behavior. The particles are most distinctly visible close to the sample surface, while they appear to evaporate quickly as they travel downstream. Observations of similar blue particles were also made by Agrawal et al. when exposing samples of an iron meteorite (Campo Del Cielo) in the Interaction Heating Facility (IHF) at NASA Ames Research

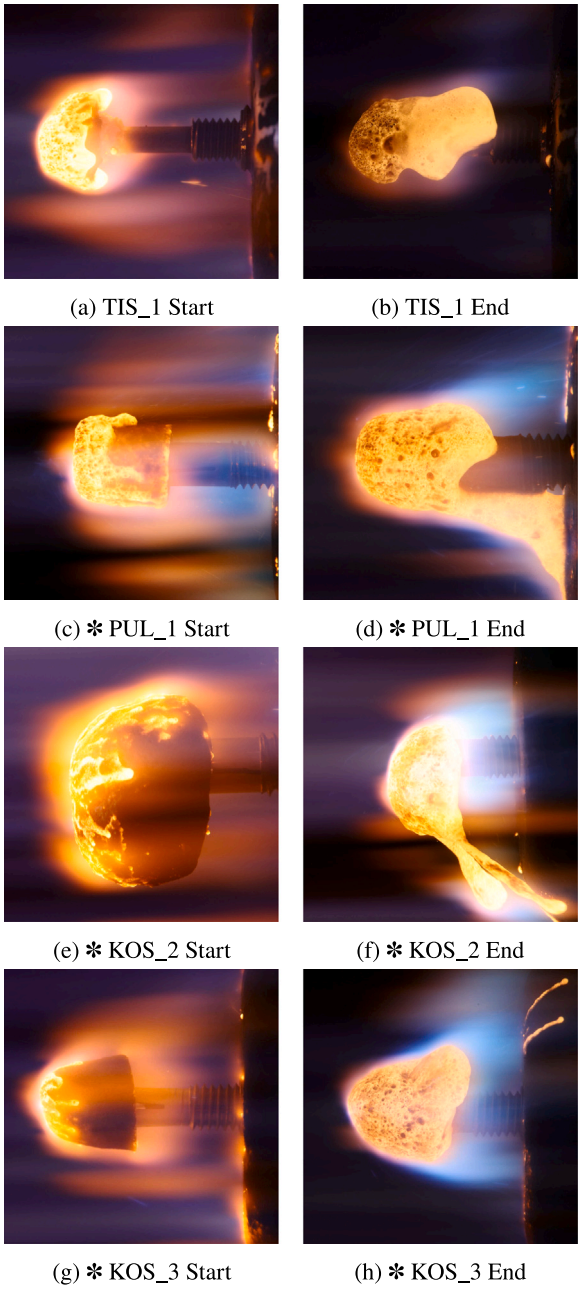

Fig. 5. Medium viscosity samples (continued from Figs. 3 and 4). The ✻ symbol indicates the observation of blue particles in the experiment.

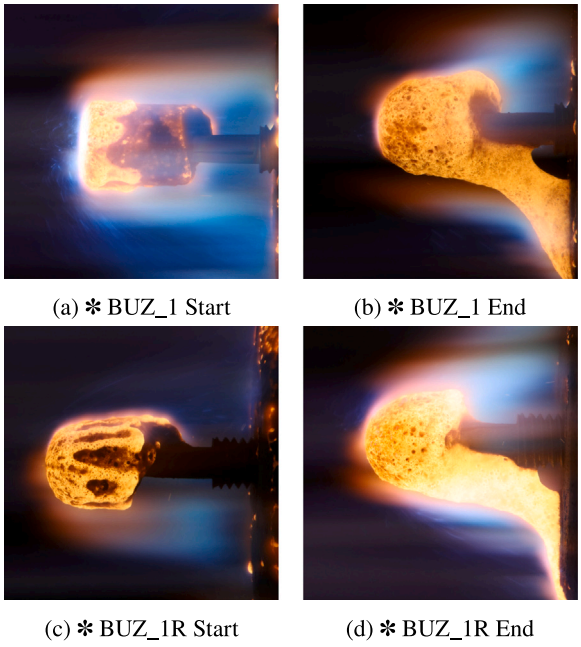

Fig. 6. Medium viscosity samples (continued from Figs. 3–5). The ✻ symbol indicates the observation of blue particles in the experiment.

Center (Agrawal et al., 2018). In these experiments the average heat flux and stagnation pressure of more than 32 MW/m^2 and 1260 hPa respectively were well above the conditions used in our experiments (see Table 1). Table 3 shows a list of the experiments during which a significant number of blue particles was observed.

The high-resolution images of the meteorites show particles being ejected from the meteorite surfaces. There are mainly two types of particles visible in the images: Medium sized particles that appear to be visible mainly due to thermal radiation and smaller blue particles that, if present, are often more numerous than the other particles. The blue particles appear to even travel small distances upstream.

An application of automated particle detection algorithms as used in engineering problems of ablation (e.g. Davuluri et al., 2023 or Martin et al., 2016) are not applicable in the present case, because the bright emission of the plasma flow around the meteorite sample disturbs the automatic detection. Therefore the particles were counted manually in the DSLR images. It was shown in previous studies that manual counting is close to automatic counting (Vaubaillan et al., 2023). Nevertheless, the number of identified particles serves as a qualitative measure to describe the overall deconstruction behavior. The particle counting was done by placing markers on each particle or trajectory in every image and then summing the number of markers. Each particle was only counted once by marking the initial point of the trajectory in each image. Some particles also split up into smaller fragments along their trajectory. Only the initial particle was counted in those cases. To increase the visibility of ejected particles, unsharp masking was applied on the images first. The improved contrast through this method is shown in Fig. 8. However, especially these numbers are to be treated carefully, as many particles evaporate along their trajectory and cannot always be distinctly identified.

The results from the particle counting are shown in Table 4 with the iron content from Table 2 given again for comparison. The most striking observation is that close to no particles were found in the images of most achondrites. Meteorites with a high iron content tend to release more particles. A comparison with Table 3 suggests that the blue particles consist of iron rich material. This is also supported by the fact that by far the most blue particles were identified during the experiment of sample MJO, which consists of approx. 92.72% of iron. However, not all experiments support this trend. For example, meteorite MUR with an iron content of 22.24% showed close to no blue particles, though with a large number of orange particles it had the second highest particle count per image. Meteorite MIN on the other hand showed plenty of blue particles though with 11.2% it has a lower iron content than SAR (14.5%) or STA (13.95%), for which negligible numbers of particles were seen. It should be noted that the Fe content taken from the literature for the Mincy meteorite is quite low compared to average Fe contents of mesosiderites. It is possible that the assumed Fe content of the tested Mincy sample is in fact too low. Another possible explanation for the abundance of blue particle in the Mincy experiment could be differences in the way that iron is bound within the material. The iron could be present in metal form

Table 4
Results of the manual particle identification.
Source: The density values are taken from Tóth et al. (2023).

Code	Name	Classification	Bulk density [g cm^{-3}]	Fe content [%]	Particles/Image
LUN	NW Africa 11303	Lunar brecchia	3.0	3.31	0.2
NCO	Norton County	Aubrite	2.7	1.67	0.76
BIL	Bilanga	Diogenite	3.0	10.50	1.25
STA	Stannern	Eucrite	2.9	13.95	1.50
SAR	Sarcicisek	Howardite	2.97	14.50	1.89
TIS	Tissint	Shergottite	3.0	15.34	4.80
ALL	Allende	CV	2.86	23.16	9.45
KNY_1R	Knyahinya	LL5	3.22	20.8	14.20
KLJ	Kheneg Ljouad	LL 5/6	3.22	18.50	15.56
CHE	Chelyabinsk	LL5	3,3	19.20	17.73
MOC	Mocs	L5	3.2	22.49	20.14
RAG_2	Ragland	LL3	3.3	20.00	22.59
NWA_1R	NW Africa 869	L5	3.36	22.11	23.88
RAG_1	Ragland	LL3	3.3	20.00	26.13
KOS_3	Kosice	H5	3.43	28.86	30.75
LAN	Lancé	CO	3.3	25.33	34.60
KNY_1	Knyahinya	LL5	3.35	20.80	35.10
NWA_1	NW Africa 869	L5	3.36	22.11	35.80
BUZ_1R	Buzzard Coulee	H5	3.5	27.50	41.87
DHO	Dhofar 1575	Ureilite	3.19	14.76	45.50
EAG	Eagle	EL	4.8	23.19	49.00
KOS_2	Kosice	H5	3.43	28.86	56.34
PUL	Pultusk	H5	3.49	27.21	65.41
BUZ_1	Buzzard Coulee	H4	3.5	27.50	67.95
MIN	Mincy	Mesosiderite	4.2	11.20	74.80
MUR	Murchison	CM	2.25	22.24	84.75
MJO	Mount Joy	Octahedrite	7.8	92.92	150.20

but also as iron oxides or sulfites (Wilkison and Robinson, 2000; Tóth et al., 2023). A more in-depth analysis of the meteorite composition, microstructure and the release mechanisms of the different elements would be needed. Pittarello et al. concluded from wind tunnel testing that oxidation of iron is an important process for the melt evolution. A clear conclusion of the melting process with respect to the iron content cannot be given from our experiments.

The effect of Fe on particle ejection is further emphasized in Fig. 9. Since the relative Fe composition and Si composition are inversely correlated, a direct comparison of the relative compositions with the number of particles does not allow to conclude, whether the blue particles are caused by an abundance of Fe or a lack of Si. To decouple the effect of Fe and Si on the particle distribution, the relative composition values of Table 2 were multiplied by the bulk densities from Table 4, which yields the elemental densities of Fe and Si. Figs. 9(a) and 9(b) show the same particle numbers from Table 4 plotted over the relative density of Fe and Si, respectively. The shapes of the markers indicate the meteorite type and the color denotes the apparent viscosity (high, medium, or low) as it was categorized based on the DSLR images. Filled markers indicate a large abundance of blue particles.

The achondrites with their low iron content stand out with a low particle count. The meteorites from the high- and medium-viscosity groups suggest a slight trend of increasing particle counts with increased iron content. The meteorites which released blue particles tend to have both the highest Fe density and the highest particle count. The carbon rich samples MUR and DHO present outliers, as they released many droplets but no blue particles. Hence, their particle count is not related to iron density. The assumed Fe content of MIN contains high uncertainties, which might be a reason why it does not follow the trend of the other samples. As discussed above, these results support the assumption that the numerous blue particles stem from iron-rich material. However, the correlation of the number of particles with the bulk density in Fig. 10 shows a trend similar to the correlation with the iron density. From this plot, it could be concluded that a larger bulk density leads to more particles being spalled from the meteorite. At this point there is no clear explanation for this observation. Fig. 9(b) shows no significant correlation of the number of particles with the Si density.

6. Conclusion

A set of 32 ablation experiments was conducted from samples from 28 different meteorites in the plasma wind tunnel PWK1 in three separate test campaigns. The diagnostic setup included several high-resolution DSLR cameras for a detailed visual analysis of the melting and ablation behavior of the meteorites. In this paper, the images were analyzed with respect to the apparent rheological behavior and the tendency to fragment and the development of particles. For some meteorites, the bulk of molten material remained mostly connected to the main body, which is attributed to higher viscosity. Other meteorites experienced a stronger flow of molten material downstream, which lead to long bulks of material forming in the back of the samples. For the samples from the two most carbon rich meteorites Murchison and Dhofar 1575 the flow of molten material along the sample surface suggested an especially low viscosity. Many droplets of molten material were seen in the images of these two samples. These results emphasize that the role of carbon on the melting and ablation behavior of meteorites should be considered for modeling fragmentation of carbonaceous meteoroids in the atmosphere. For many meteorites the release of small blue particles was also observed. Unlike the droplets of molten material,

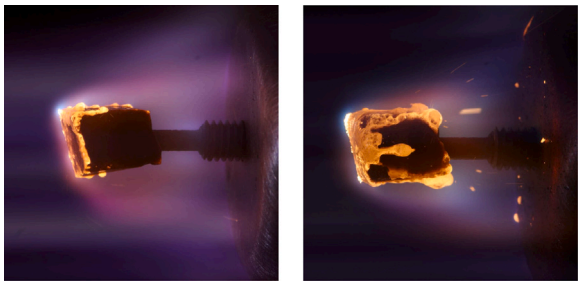

(a) DHO_1 Start (b) DHO_1 End

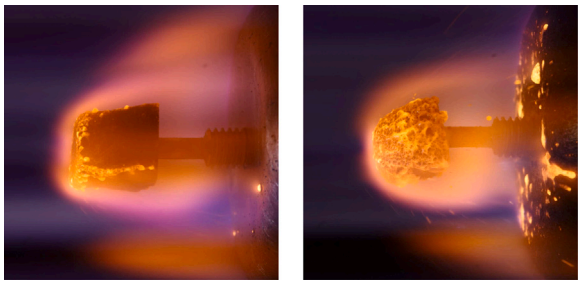

(c) MUR_1 Start (d) MUR_1 End

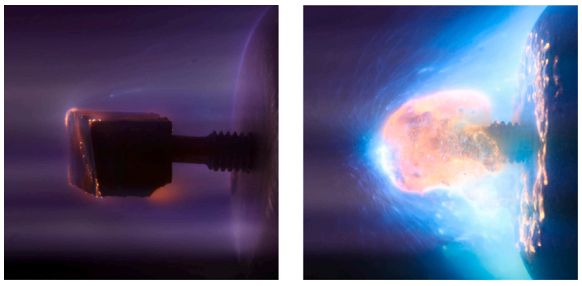

(e) ✻ MJO_1 Start (f) ✻ MJO_1 End

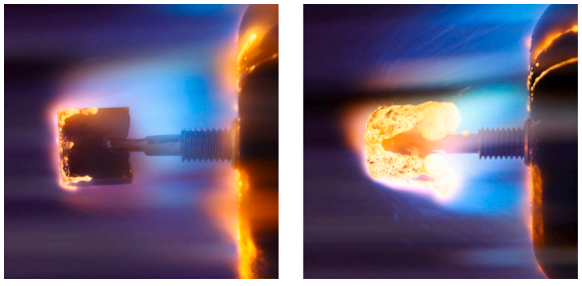

(g) ✻ MIN_1 Start (h) ✻ MIN_1 End

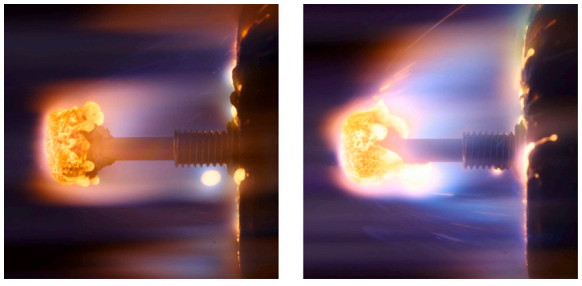

(i) ✻ LAN_1 Start (j) ✻ LAN_1 End

Fig. 7. Low viscosity samples. The ✻ symbol indicates the observation of blue particles in the experiment.

these particles also traveled a few millimeters upstream after being ejected from the surface and quickly evaporated in the plasma flow. An analysis of the meteorite compositions suggested that these blue particles mainly consist of iron. Most achrondites consistently showed close to no release of particles or droplets.

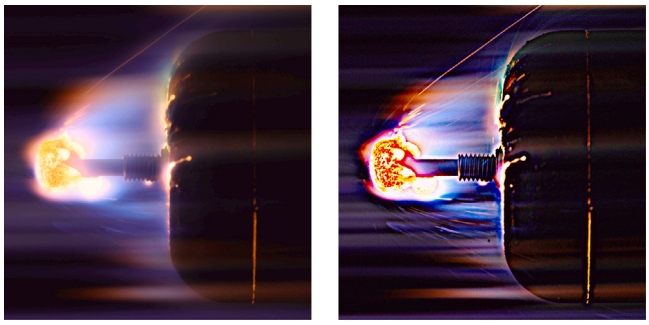

(a) Original image (b) Filtered image

Fig. 8. Unsharp masking of an image of the LAN meteorite. This improved the visibility of the particles.

CRediT authorship contribution statement

F. Grigat: Writing – original draft, Visualization, Methodology, Investigation. **S. Loehle:** Writing – review & editing, Supervision, Investigation, Funding acquisition, Formal analysis, Data curation. **J. Vaubaillon:** Methodology, Investigation, Funding acquisition, Formal analysis. **P. Matlovič:** Supervision, Project administration. **J. Tóth:** Project administration, Funding acquisition.

Declaration of competing interest

The authors declare the following financial interests/personal relationships which may be considered as potential competing interests: Felix Grigat reports financial support was provided by European Space Agency. Stefan Loehle reports financial support was provided by European Space Agency. Pavol Matlovic reports financial support was provided by Slovak Grant Agency for Science. Juraj Toth reports financial support was provided by Slovak Grant Agency for Science. Jeremie Vaubaillon reports financial support was provided by French Space Agency.

Data availability

Data will be made available on request.

Acknowledgments

This work was supported by the European Space Agency (ESA) ESA contract No. 4000128930_19_NL_SC. J. Tóth and P. Matlovič were supported by the Slovak Research and Development Agency grant APVV-16-0148 and the Slovak Grant Agency for Science grant VEGA 1/0218/22. J. Vaubaillon was supported by CNES, the French Space Agency, in the framework of the MALBEC project. We thank Ludovic Ferrière from the Natural History Museum Vienna for providing meteorite samples used in the experiments. The authors thank the HEFDiG team for the support in the experiments and the review of the paper. We would also like to thank Daniel Britt from the Center for Lunar and Asteroid Surface Science and Jérôme Gattacceca from the French National Centre for Scientific Research for the valuable discussions.

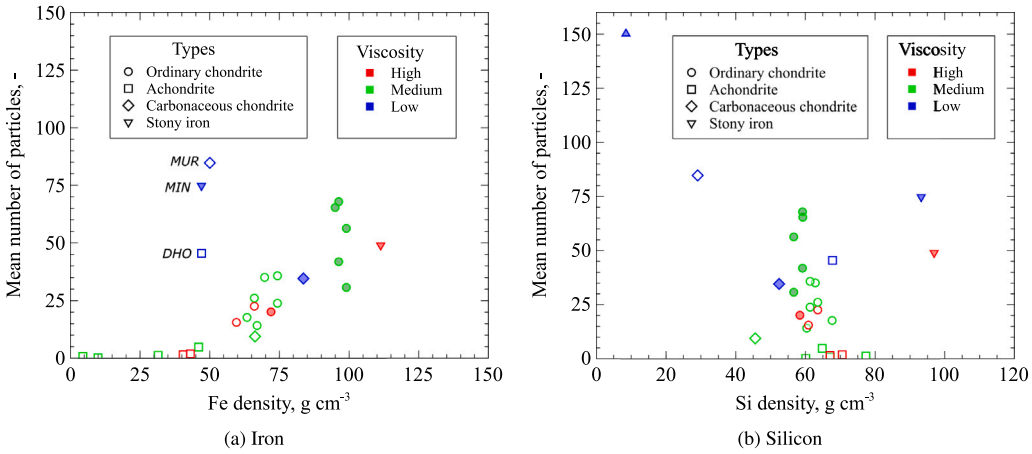

Fig. 9. Average number of particles per image plotted against the elemental densities of Fe and Si. Filled markers indicate a large abundance of blue particles.

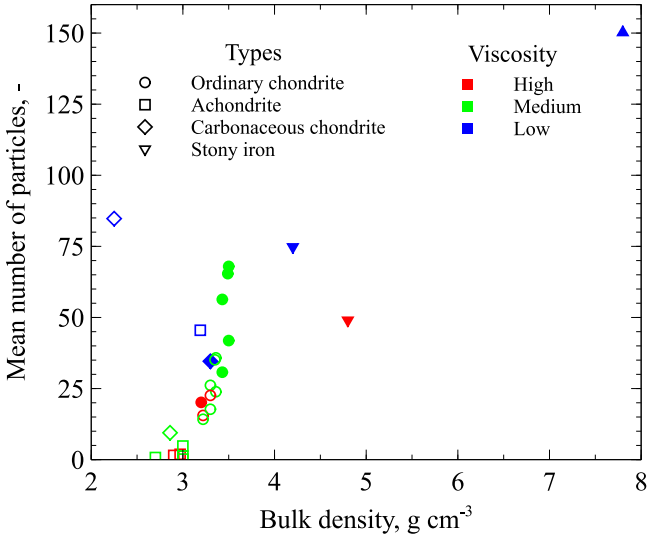

Fig. 10. Average number of particles per image plotted against the bulk density. Filled markers indicate a large abundance of blue particles.

References

Agrawal, P., Jenniskens, P., Stern, E., Arnold, J., Chen, Y.-K., 2018. Arcjet ablation of stony and iron meteorites. In: 2018 Aerodynamic Measurement Technology and Ground Testing Conference. AIAA, Reston, VA, USA, http://dx.doi.org/10.2514/6.2018-4284.

Barrat, J.A., Yamaguchi, A., Greenwood, R.C., Benoit, M., Cotten, J., Bohn, M., Franchi, I.A., 2008. Geochemistry of diogenites: Still more diversity in their parental melts. Meteorit. Planet. Sci. 43 (11), 1759–1775. http://dx.doi.org/10.1111/j.1945-5100.2008.tb00641.x.

Bethe, 1959. A theory for the ablation of glassy materials. J. Aerosp. Sci. 26 (6), 321–328. http://dx.doi.org/10.2514/8.8080.

Davuluri, R., Price, K.J., Bailey, S., Tagavi, K., Martin, A., 2023. Numerical reconstruction of spalled particle trajectories in an arc-jet environment: Accounting for non-sphericity and back-tracking. In: SciTech 2023 Forum. American Institute of Aeronautics and Astronautics, Reston, VA, USA, http://dx.doi.org/10.2514/6.2023-2714.

Easton, A.J., 1985. Seven new bulk chemical analyses of aubrites. Meteoritics 20 (3), 571–573. http://dx.doi.org/10.1111/j.1945-5100.1985.tb00052.x.

Flynn, G.J., 2002. Extraterrestrial dust in the near-earth environment. Meteors Earth's Atmos. 77–94.

Giordano, D., Russell, J.K., Dingwell, D.B., 2008. Viscosity of magmatic liquids: A model. Earth Planet. Sci. Lett. 271 (1–4), 123–134.

Goodrich, C.A., Hartmann, W.K., O'Brien, D.P., Weidenschilling, S.J., Wilson, L., Michel, P., Jutzi, M., 2015. Origin and history of ureilitic material in the solar system: The view from asteroid 2008 TC 3 and the almahata sitta meteorite. Meteorit. Planet. Sci. 50 (4), 782–809.

Grigat, F., Loehle, S., Zander, F., Fasoulas, S., 2022. Spallation on carbon ablators. AIAA J. 60 (7), 3936–3949. http://dx.doi.org/10.2514/1.J061276.

Helber, B., Dias, B., Bariselli, F., Zavalan, L., Pittarello, L., Goderis, S., Soens, B., McKibbin, S.J., Claeys, P., Magin, T.E., 2019. Analysis of meteoroid ablation based on plasma wind-tunnel experiments, surface characterization, and numerical simulations. Astrophys. J. 876 (2), http://dx.doi.org/10.3847/1538-4357/ab16f0.

Herd, C.D.K., Duke, M.J.M., Bryden, C.D., Pearson, D.G., 2013. Tissint among the shergottites: Parental melt composition, redox state, La/Yb and V/Sc. In: 44th Lunar and Planetary Science Conference.

Hui, H., Zhang, Y., 2007. Toward a general viscosity equation for natural anhydrous and hydrous silicate melts. Geochim. Cosmochim. Acta 71 (2), 403–416.

Jarosewich, E., 1971. Chemical analysis of the murchison meteorite. Meteoritics 6 (1), 49–52. http://dx.doi.org/10.1111/j.1945-5100.1971.tb00406.x.

Jarosewich, E., Clarke, R.C., Barrows, J.N., 1987. Allende meteorite reference sample. Smithson. Contr. Earth Sci. (27), 1–49. http://dx.doi.org/10.5479/si.00810274.27.1.

Jenniskens, P., 2006. Meteor Showers and Their Parent Comets. Cambridge University Press, Cambridge.

Jenniskens, P., Nénon, Q., Albers, J., Gural, P.S., Haberman, B., Holman, D., Morales, R., Grigsby, B.J., Samuels, D., Johannink, C., 2016. The established meteor showers as observed by CAMS. Icarus 266, 331–354.

Kallemeyn, G.W., Rubin, A.E., Wang, D., Wasson, J.T., 1989. Ordinary chondrites: Bulk compositions, classification, lithophile-element fractionations and composition-petrographic type relationships. Geochim. Cosmochim. Acta 53 (10), 2747–2767. http://dx.doi.org/10.1016/0016-7037(89)90146-4.

Kirillov, A., Grozdov, D., Zinicovscaia, I., Vasilenko, T., 2022. Elemental composition of the chelyabinsk meteorite determined by neutron activation analysis. J. Radioanal. Nucl. Chem. 331 (1), 249–253. http://dx.doi.org/10.1007/s10967-021-08078-z.

Kitts, K., Lodders, K., 1998. Survey and evaluation of eucrite bulk compositions. Meteorit. Planet. Sci. 33 (S4), A197–A213. http://dx.doi.org/10.1111/j.1945-5100.1998.tb01334.x.

Kolesnikov, A.F., 1999. Extrapolation from high enthalpy tests to flight based on the concept of local heat transfer simulation. In: RTO Educational Notes 8. NATO, Neuilly-sur-Seine, France.

Kusuno, H., Fukuoka, T., Matsuzaki, H., 2013. Simple relationship between 26Al production rate and major elemental composition of meteorite samples. Geochem. J. 47 (1), 83–88. http://dx.doi.org/10.2343/geochemj.2.0239.

Leiser, D., Duernhofer, C., Poloni, E., Loehle, S., Matlovič, P., Tóth, J., Vaubaillan, J., 2023. Meteorite temperature measurements during ground testing. In: Feaga, L. (Ed.), ICARUS - Wind Tunnel Meteors. http://dx.doi.org/10.1016/j.icarus.2023.115867.

Lewis, C.F., Moore, C.B., 1971. Chemical analyses of thirty-eight iron meteorites*. Meteoritics 6 (3), 195–205. http://dx.doi.org/10.1111/j.1945-5100.1971.tb00111.x.

Loehle, S., Brandis, A., Hermann, T., Peter, J., 2012. Numerical investigation of the re-entry flight of hayabusa and comparison to flight and ground testing data. In: 43rd AIAA Thermophysics Conference. AIAA, Reston, VA, USA, http://dx.doi.org/10.2514/6.2012-3102.

Loehle, S., Vaubaillan, J., Matlovič, P., Tóth, J., 2023. Meteorite material luminous efficiencies from ground testing of meteoroid entry. In: Feaga, L. (Ed.), ICARUS - Wind Tunnel Meteors. http://dx.doi.org/10.1016/j.icarus.2023.115817.

Loehle, S., Zander, F., Hermann, T., Eberhart, M., Meindl, A., Oefele, R., Vaubaillan, J., Colas, F., Vernazza, P., Drouard, A., Gattacceca, J., 2017. Experimental simulation of meteorite ablation during earth entry using a plasma wind tunnel. Astrophys. J. 837 (2), http://dx.doi.org/10.3847/1538-4357/aa5cb5.

Martin, A., Bailey, S.C.C., Panerai, F., Davuluri, R.S.C., Zhang, H., Vazsonyi, A.R., Lippay, Z.S., Mansour, N.N., Inman, J.A., Bathel, B.F., Splinter, S.C., Danehy, P.M., 2016. Numerical and experimental analysis of spallation phenomena. CEAS Space J. 8 (4), 229–236. http://dx.doi.org/10.1007/s12567-016-0118-4.

Mason, B., Wiik, H.B., 1961. The Composition of the Ottawa, Chateau-Renard, Mocs, and New Concord Meteorites. Am. Mus. Novitates (2069).

McCarthy, T.S., Erlank, A.J., Willis, J.P., 1973. On the origin of eucrites and diogenites. Earth Planet. Sci. Lett. 18 (3), 433–442. http://dx.doi.org/10.1016/0012-821X(73)90100-3.

Metzler, K., Bischoff, A., Greenwood, R.C., Palme, H., Gellissen, M., Hopp, J., Franchi, I.A., Trieloff, M., 2011. The L3-6 chondritic regolith breccia northwest Africa (NWA) 869: (I) petrology, chemistry, oxygen isotopes, and Ar-Ar age determinations: The L3-6 chondritic regolith breccia NWA 869: (I). Meteorit. Planet. Sci. 46 (5), 652–680. http://dx.doi.org/10.1111/j.1945-5100.2011.01181.x.

Mittlefehldt, D.W., Chou, C.-L., Wasson, J.T., 1979. Mesosiderites and howardites: igneous formation and possible genetic relationships. Geochim. Cosmochim. Acta 43 (5), 673–688. http://dx.doi.org/10.1016/0016-7037(79)90252-7.

Miura, Y., Iancu, G.O., Iancu, G., Yanai, K., Haramura, H., 1995. Reexamination of mocs and tauti chondritic meteorites: Classification with shock degree. Antarct. Meteor. Res. 8, 153.

Olsen, E.J., Huss, G.I., Jarosewich, E., 1988. The eagle, nebraska enstatite chondrite (EL6). Meteoritics 23 (4), 379–380. http://dx.doi.org/10.1111/j.1945-5100.1988.tb00928.x.

Ozdín, D., Plavčan, J., Horňáčková, M., Uher, P., Porubčan, V., Veis, P., Rakovský, J., Tóth, J., Konečný, P., Svoreň, J., 2015. Mineralogy, petrography, geochemistry, and classification of the košice meteorite. Meteorit. Planet. Sci. 50 (5), 864–879. http://dx.doi.org/10.1111/maps.12405.

Panerai, F., Bessire, B., Haskins, J., Foster, C., Barnard, H., Stern, E., Feldman, J., 2021. Morphological evolution of ordinary chondrite microstructure during heating: implications for atmospheric entry. Planet. Sci. J. 2 (5), 179.

Park, C., Brown, J.D., 2012. Fragmentation and spreading of a meteor-like object. Astron. J. 144 (6), 184. http://dx.doi.org/10.1088/0004-6256/144/6/184.

Pearson, V.K., Sephton, M.A., Franchi, I.A., Gibson, J.M., Gilmour, I., 2006. Carbon and nitrogen in carbonaceous chondrites: Elemental abundances and stable isotopic compositions. Meteorit. Planet. Sci. 41 (12), 1899–1918.

Phelan, N., Day, J.M.D., Dhaliwal, J.K., Liu, Y., Corder, C.A., Strom, C., Pringle, E., Assayag, N., Cartigny, P., Marti, K., Moynier, F., 2022. A 187Re-187os, 87Rb-87Sr, highly siderophile and incompatible trace element study of some carbonaceous, ordinary and enstatite chondrite meteorites. Geochim. Cosmochim. Acta 318, 19–54. http://dx.doi.org/10.1016/j.gca.2021.11.020.

Pisarčíková, A., Matlovič, P., Tóth, J., Loehle, S., Ferrière, L., Leiser, D., Grigat, F., Vaubaillan, J., 2023. Analysis of CN emission as a marker of organic compounds in meteoroids using maboratory meteor data. In: Feaga, L. (Ed.), ICARUS - Wind Tunnel Meteors.

Recca, S.I., Scott, E., Keil, K., Clayton, R.N., Mayeda, T.K., Huss, G., Jarosewich, E., Weeks, K.S., Hasan, F.A., Sears, D., Wieler, R., Signer, P., 1986. Ragland, an ll3.4 chondrite find from New Mexico. Meteoritics 21 (2), 217–229. http://dx.doi.org/10.1111/j.1945-5100.1986.tb01243.x.

Shepard, C.E., Vorreiter, J.W., Stine, H.A., Winovich, W., 1967. A study of artificial meteors as ablators: Technical report.

Simpson, A.B., Ahrens, L.H., 1977. 5. The chemical relationship between howardites and the silicate fraction of mesosiderites. Int. Astron. Union Colloq. 39, 445–450. http://dx.doi.org/10.1017/S0252921100070391.

Tóth, J., Matlovič, P., Loehle, S., Vaubaillon, J., Pisarčíková, A., Leiser, D., Grigat, F., Eberhart, M., Hufgard, F., Ravichandran, R., Poloni, E., Hoerner, I., Duernhofer, C., Delahaie, S., Ferrière, L., Rommeluere, S., Rambaux, N., 2023. Overview of MetSpec project – from laboratory ablated meteorite to meteor spectroscopy. In: Feaga, L. (Ed.), ICARUS - Wind Tunnel Meteors. http://dx.doi.org/10.1016/j.icarus.2023.115791.

Unsalan, O., Jenniskens, P., Yin, Q.-Z., Kaygisiz, E., Albers, J., Clark, D.L., Granvik, M., Demirkol, I., Erdogan, I.Y., Bengu, A.S., Özel, M.E., Terzioglu, Z., Gi, N., Brown, P., Yalcinkaya, E., Temel, T., 2019. The sariçiçek howardite fall in Turkey: Source crater of HED meteorites on vesta and impact risk of vestoids. Meteorit. Planet. Sci. 54 (5), 953–1008. http://dx.doi.org/10.1111/maps.13258.

Vaubaillan, J., Loir, C., Ciocan, C., Kandeepan, M., Millet, M., Cassagne, A., Lacassagne, L., Da Fonseca, P., Zander, F., Buttsworth, D., Loehle, S., Tóth, J., Gray, S., Moingeon, A., Rambaux, N., 2023. A 2022 tau -herculid meteor cluster from an airborne experiment: automated detection, characterization, and consequences for meteoroids. Astron. Astrophys. 670, A86. http://dx.doi.org/10.1051/0004-6361/202244993.

Wasson, J.T., 1969. The chemical classification of iron meteoritesIII. Hexahedrites and other irons with germanium concentrations between 80 and 200 Ppm. Geochim. Cosmochim. Acta 33 (7), 859–876. http://dx.doi.org/10.1016/0016-7037(69)90032-5.

Wilkison, S.L., Robinson, M.S., 2000. Bulk density of ordinary chondrite meteorites and implications for asteroidal internal structure. Meteorit. Planet. Sci. 35 (6), 1203–1213.